Order-disorder transition in amorphous vanadium-phosphorus-lithium cathode of lithium ion battery

Kong, F., Sun, D., Rao, Y., Zhang, R., Chen, Z., Wang, D., Yu, X., Jiang, H., & Li, C. (2022). Order-disorder transition in amorphous vanadium-phosphorus-lithium cathode of lithium ion battery. *Applied Surface Science*, *573*, Article 151490. https://doi.org/10.1016/j.apsusc.2021.151490

Published in:
Applied Surface Science

Document Version:
Peer reviewed version

Order-disorder Transition in Amorphous Vanadium-Phosphorus-Lithium Cathode of Lithium Ion Battery

Fanhou Kong[a,b,c], Dan Sun[b], Yinzhao Rao[a], Ruixiang Zhang[a], Zelin Chen[a], Dan Wang [a], Xiaolong Yu[a,c], Hong Jiang[a,c], Changjiu Li[a,c,*]

[a]State Key Laboratory of Marine Resource Utilization in South China Sea (Hainan University)&Special Glass Key Lab of Hainan Province, Haikou, 570228, P. R. China

[b]School of Mechanical and Aerospace Engineering, Queen's University Belfast, Belfast, BT9 5AH, UK

[c]Key Laboratory of Advanced Materials of Tropical Island Resources of Ministry of Education, Haikou, 570228, P. R. China

∗ Corresponding author

Changjiu Li:State Key Laboratory of Marine Resource Utilization in South China Sea (Hainan University)&Special Glass Key Lab of Hainan Province, Haikou, 570228, China. E-mail addresses: **lichangjiu@hainanu.edu.cn.**

Highlights

- The effect of fluorination on the order-disorder transition of vanadium-phosphorus-lithium amorphous lithium (VPLi) battery cathode has been investigated for the first time.
- Li_3VF_6 and VF_4 nanocrystals were found to precipitate from VPFLi when V^{4+} content is ranged from 16.3% to 23.8%.
- VF_4 and Li_3VF_6 nanocrystals were converted into $LiVP_2O_7$ in VPFLi, which led to the increased specific capacity of the resulting cathode.
- Density functional theory (DFT) simulation results show that fluorination has led to the movement of Fermi level towards the edge of the conduction band, and the charge transfer from Li to O contributed to the enhanced cycle stability.

A B S T R A C T

Vanadium-based amorphous materials are an emerging category of lithium ion battery cathodes with high specific capacity and high voltage performance. In this study, we investigated the effect of fluorination on the performance of an amorphous vanadium-phosphorus-lithium (VPLi) cathode for lithium ion battery applications. Results show that the fluorinated product consists Li_3VF_6 and VF_4 nanocrystals embedded in an amorphous phase when the V^{4+} content was in the range of 16.3% to 23.8%. VPFLi has an optimal

specific capacity of 344.3 mAh g^{-1} in the first cycle and 269.7 mAh g^{-1} after 200 cycles at a current of 50 mA g^{-1} within the voltage range of 1.5-4.2V. VPLi has an amorphous structure, and the reversible V^{4+}/V^{5+} lithiation process corresponds to the conversion between V_2O_5 and $Li_2V_2O_5$ during the charge-discharge cycle. Compared to VPLi, VF_4 and Li_3VF_6 crystals were found to convert into $LiVP_2O_7$ in VPFLi, which led to the increased specific capacity. Simulation based on density functional theory show that fluorine for oxygen has led to the movement of Fermi level moves towards the edge of the conduction band. Charge mostly transferred from Li to O which contributed to the improved cathode stability. This study provides a new perspective towards selecting novel cathode for lithium-ion batteries.

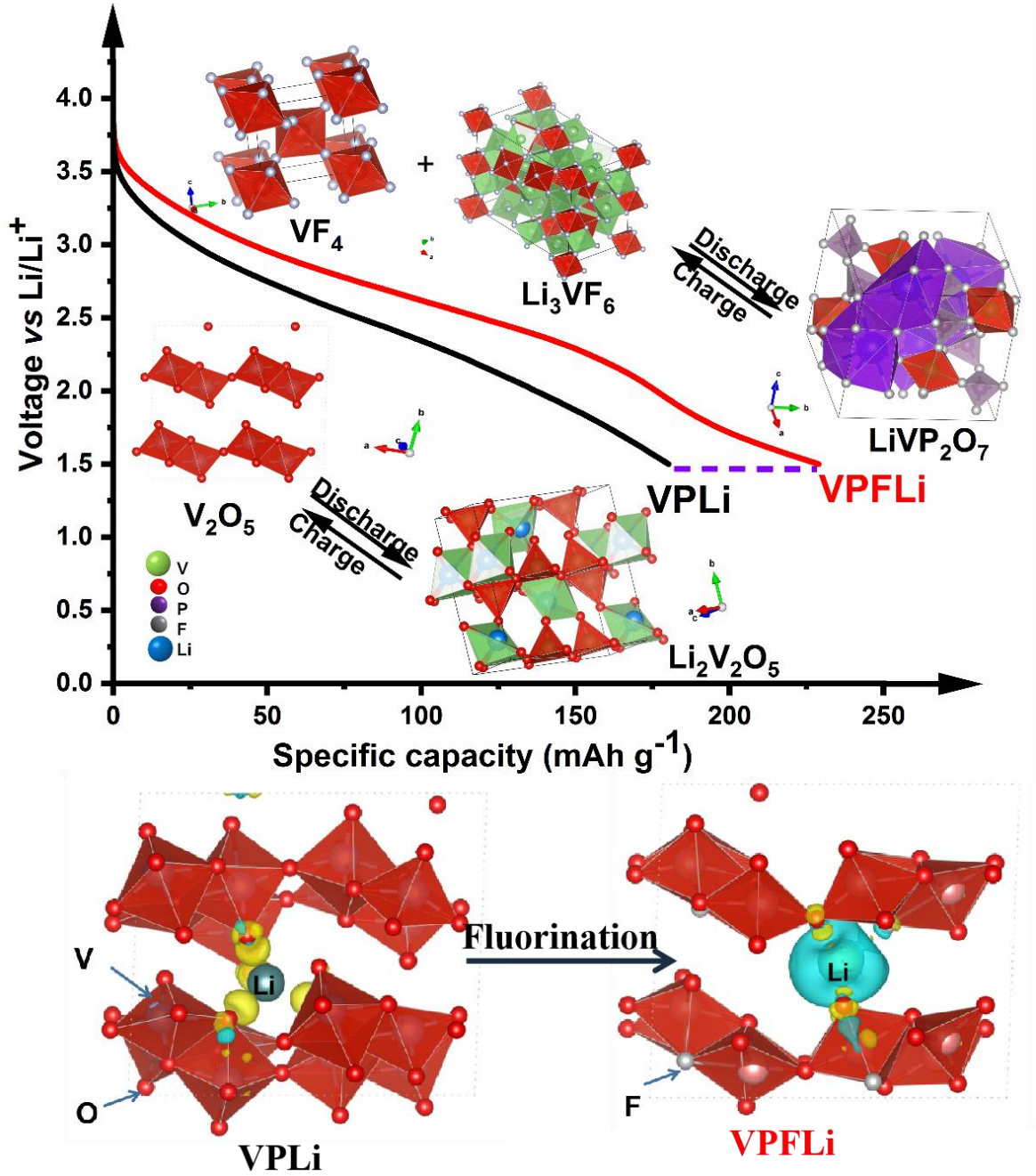

GRAPHICAL ABSTRACT

Keywords

Lithium-ion battery; Vanadium; Cathode; Fluorination; Order-disorder transition;

1. Introduction

Due to the global energy challenge, low cost and high efficiency energy conversion / storage are becoming increasingly important in today's society [1-4]. The global energy harvesting system market accounted for $449.75 million in 2019 and is expected to reach $1,097.77 million by 2027 [5]. Lithium ion batteries are widely used in energy harvesting because of their high specific capacity and cycle stability [6-9].

However, conventional cathode materials such as $LiFePO_4$ [10] and NCM (Ni, Co, and Mn) -based materials [11] suffer from low specific capacity, lack of natural supplies and high cost. Transition metals (TM), such as vanadium-based compounds [12-14] (e.g. V_2O_5), are promising alternatives [15] due to their abundant natural supply source, multivalent states (V^{2+}-V^{5+}), and high specific capacity [16-19]. However, V_2O_5 being an amphoteric acid-base, has limitations such as high dissolution rate, irreversible phase change, severe volume expansion, and low electronic conductivity [20-22].

As a result, many strategies have been explored to improve the performance of vanadium-based electrode materials, such as deploying multi-dimensional structures [18.23.24], disordered rock salt [25-29], conductive coating [30-33], valence transition [34-38], and phase transformation [39-41], etc.

However, in contrast to the mature crystalline based lithium battery electrode material technologies, the performance and working mechanism of amorphous electrode materials are far less understood. In recent years, amorphous glass materials [42-44] have received increasing attention in lithium battery electrode development. Y. Zhang and Y. Yue et al [45] explored the structural factors that affect the electrochemical performance of glass anodes, especially the structural evolution during the discharge-charge process. In a separate study, they [46] found that the structural network of the electrode can be dissociated into isolated units through solid-state nuclear magnetic resonance, and form different types of highly ordered

nano-domains, which led to favorable rate capability and long-term cycle stability. H. Tao and Y. Yue et al [47] succeeded in tuning the degree of disorder in NaFePO4 cathode material by a mechanochemical route, thereby obtaining the excellent cycling stability. To date, applications of vanadium oxide-based amorphous glass electrode materials have been reported by several research groups, examples include vanadium-phosphorus [48-50], vanadium-boron [51], vanadium-tellurium [52-54], and vanadium-silicon[55], etc. Due to the lack of accurate *in situ* characterization for amorphous electrode structure, the current research mostly focus on the composition-performance improvement, and the results cannot track the cycle process, reveal the lithiation mechanism, or support theoretical calculations.

Oxygen pairs, short-range O-O bonds and the formation of oxygen vacancies can lead to the voltage drop and capacity degradation during long term cycling of the cathode [56]. Due to the greater electronegativity of F (4.0) as compared to O (3.5), F has a stronger ability to attract electrons. In this work, we reported the first study on fluorine-oxygen substitution in an amorphous lithium-ion battery cathode system. An amorphous vanadium-phosphorus-lithium cathode material (VPLi) and its fluorinated product (VPFLi) were prepared by melting quenching method. Specifically, the thermodynamic properties of both materials were characterized to reveal the difference in their lithiation mechanisms. This is followed by detailed evaluation using DSC, *in situ* XRD, FT-IR, Raman, SEM, TEM, NMR, XPS, and EPR. The order /disorder phase transformation in the fluorinated amorphous electrode material were revealed. The cathode materials electrochemical properties, including their specific capacity, rate performance, long-term cycling, have been assessed and compared using a practical lithium-ion battery cell set up. Finally, DFT calculations were performed to reveal the difference in the charge density distribution between the electrode materials with and without fluorination.

2. Methodology

2.1. Materials Preparation

Amorphous vanadium-phosphorus-lithium cathode materials with and without fluorine-oxygen substitution were prepared by melting-quenching method [48]. VPLi was prepared by mixing raw materials

Li_3PO_4 (Macklin, CP, 99.0%) / V_2O_5 (Macklin, AR, 99.99%) with a molar ratio of 4:6, using a vertical mixer for 30 min. The mixture was placed into an alumina crucible, heated in a tube furnace under Ar atmosphere to 700 ℃ at a rate of 10 ℃/min. The temperature was maintained at 700 ℃ for 30 min and then raised to 900 ℃ for another 10 min of heating. The end of the tube furnace is connected to the quenching box (30cm*30cm*30cm). The resulting molten liquid was passed between two copper plates and quenched in Ar to room temperature to obtain a shaped glass specimen. The glass specimen was then annealed at 225 ℃ for 400 min to relieve the residual stresses and was cooled down to room temperature naturally. The glass specimen was ground into glass powder (particle size < 10 μm) and the resultant amorphous material was named as VPLi. For fabrication of fluorinated VPFLi, a mixture of Li_3PO_4 (Macklin, CP, 99.0%), V_2O_5 (Macklin, AR, 99.99%) and LiF (Macklin, AR, 99.0%) with a molar ratio of 3:6:3 were used and the preparation process of VPFLi is the same as that of VPLi. The material preparation process is shown in Fig.1.

2.2. Characterization

Differential scanning calorimetry (DSC, NETZSCH STA449) was conducted to study the materials thermodynamic parameters under N_2, with a heating rate of 10 ℃/min. X-ray diffractometry (XRD, Rigaku, smartlab 9kw) and *in situ* high and low temperature XRD (Rigaku TTR3) were used to identify the materials crystal structures. Fourier Transform infrared spectroscopy (FT-IR, Thermo fisher Nicolet iS5) and Raman spectroscopy (HORIBA Scientific HORIBA LabRAM HR Evolution) using a laser Raman spectrometer from Renishaw plc (532 nm) were performed. Microstructure analysis was carried out by transmission electron microscopy (TEM, JEOL JEM-2100F) and scanning electron microscopy (SEM, Verios G4 UC) with an energy dispersive spectrometer (EDS, Oxford Instruments). NMR measurements of ^{19}F were performed by a 600 MHz SS-NMR spectrometer JEOL ECZ600R/S3 equipped with a 14.09 T superconducting magnet and a 3.2mm double-resonance MAS probe (JEOL RESONANCE Inc., Japan). Particle size distribution was measured by a zetasizer nano ZS90 (Malvern Instrument). X-ray photoelectron spectroscopy (XPS, AXIS Supra) with MgKα excitation source was used to detect the relative V content in

different valence states and the different coordination of O. The electron paramagnetic resonance (EPR, Bruker A320) was used to detect the unpaired electrons in the atoms or molecules to explore the structural characteristics of its surrounding environment.

2.3. Electrochemical measurements

Two different cathodes were prepared by mixing conductive carbon black (super P) and polyvinylidene fluoride (PVDF) binder with VPLi and VPFLi, respectively, at a mass ratio of 7:2:1. N-methyl pyrrolidone (NMP) (15 wt%) was added, and the mixture was ground into a slurry. The slurry was coated onto an aluminum foil, dried thoroughly under vacuum condition, and cut into 10 mm diameter disks to be used as the cathode. CR2016 type coin cells were assembled with lithium being the anode, Celgard 2025 being the separator, and an electrolyte containing 1.0 M LiPF6 in ethylene carbonate (EC), dimethyl carbonate (DMC), and ethyl methyl carbonate (EMC) with a volume ratio of 1:1:1. The entire assembly was completed in a vacuum glove box filled with Ar (H_2O and O_2 content <1 ppm). The preparation process is shown in Fig.1. Battery cycling (Land CT3001A) was conducted at a constant current of 0.1A g^{-1} and 50 mA g^{-1} to study the cycling behaviour and rate capability within a voltage range of 1.5–4.2 V. Cyclic voltammetry (CV) was performed on an electrochemical workstation (CHI660E) in a voltage range of 1.5–4.2 V, at a scan rate of 0.5 mV/s. CHI660E was used to perform electrochemical impedance spectroscopy (EIS) in a frequency range of 10^{-2}–10^{5} Hz, at an amplitude of 5 mV.

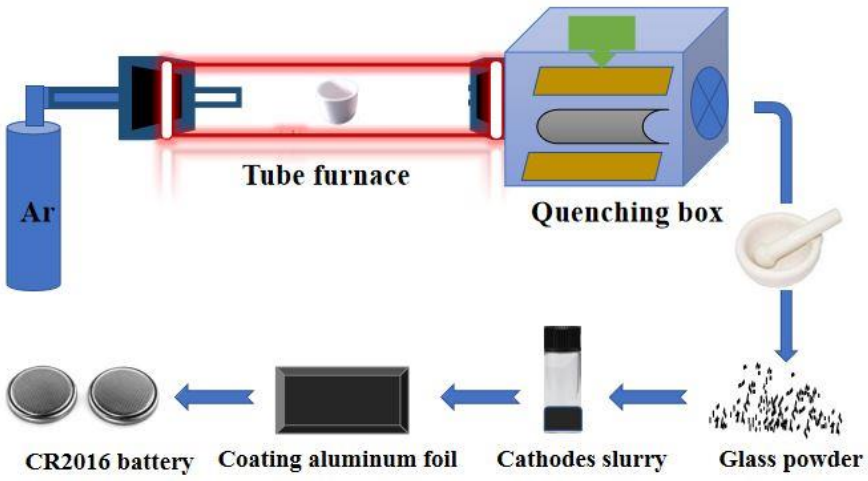

Fig.1 Schematic diagram of the material preparation process

3. Results and discussion

3.1 Structure and thermodynamic properties of fluorination on VPLi

DSC results in Fig.2(a) shows that the glass transition temperature (T_g) of VPLi was 224 ℃, with three crystal precipitation temperatures (T_C), 259 ℃ (T_{C1}), 329 ℃ (T_{C2}) and 474 ℃ (T_{C3}) and a melting temperature (T_m) of 569 ℃ (T_{m1}). The T_g of VPFLi was found to be 220 ℃, with T_{C1} and T_{C2} being 239 ℃ and 489 ℃, respectively, and T_{m1}, T_{m2} and T_{m3} being 349 ℃, 409 ℃ and 545 ℃, respectively. The lower T_C of VPFLi as compared to VPLi suggests the lower activation energy of the crystallization process required for the fluorinated system. Compared with VPLi, VPFLi has fewer crystallization peaks and more melting peaks, indicating multiple crystal systems are present in the system.

VPLi was heated and studied *in situ* using high and low temperature XRD, as shown in Fig.2(b). The sample (VPLi-25 ℃) was first heated to 270 ℃ at a rate of 10 ℃ /min and held for 30 min (VPLi-270 ℃), followed by heating to 340 ℃ at a rate of 10 ℃ /min, and maintained for 30 min (VPLi-340 ℃). Finally, the material was cooled down to room temperature naturally (VPLi-C25 ℃). Fig.2(b) shows that VPLi-25 ℃ has an amorphous phase, at elevated temperatures, VPLi-270 ℃ showed the precipitation of crystalline Li_3P (PDF#04-0525), and VPLi-340 ℃ showed precipitation of crystalline $Li_{0.3}V_2O_5$ (PDF#18-0755). The fact that VPLi possesses two potential crystal precipitation pathways suggests the material is in a thermodynamically metastable state and different heat treatment conditions can lead to precipitation of either crystalline Li_3P or $Li_{0.3}V_2O_5$. Fig.2(c) compares the XRD pattern of VPLi and VPFLi at room temperature (25 ℃). Compared to the neat amorphous VPLi, VPFLi showed ordered crystalline precipitation of VF_4 (PDF#19-1409) and Li_3VF_6 (PDF#28-0607).

Fig.2(d) shows the FT-IR spectra of VPLi, VPFLi, and as purchased Li_3PO_4, and V_2O_5. The characteristic absorption peak at 1624 cm^{-1} represents the stretching vibration of V=O. The absorption band at 1010 cm^{-1}, represents the tensile vibration of the V^{5+}=O bond [57] of VPLi, VPFLi and V_2O_5. The characteristic absorption peak at 1030 cm^{-1} represents the asymmetric stretching vibration of the tetrahedron [PO_4] [58]. The characteristic peaks at 946 cm^{-1} and 922 cm^{-1} can be correlated to the asymmetric vibration of P-O-P

[58]. of the red shift of P-O-P can be attributed to the presence of F [59].

In the subsequent Raman analysis (Fig.2(e)), the peaks at 287 and 538 cm^{-1} seen in VPLi and VPFLi can be attributed to the bending mode of the V-O-V bond [18]. Characteristic peaks such as 766 and 990 cm^{-1} are related to the tensile vibrations of the double-coordinated oxygen (V_2-O) and vanadium oxide (V=O) [18]. $\delta^{19}F$ frequency-stepping spectra (Fig.2(f)) obtained from solid-state NMR of VPFLi exhibited strong signals and chemical shifts which can be referenced against fluorotrichloromethane (CCl_3F, $\delta_{(^{19}F)}$ = 0 ppm) [26]. However, no such signal has been found in VPLi in this region [46].

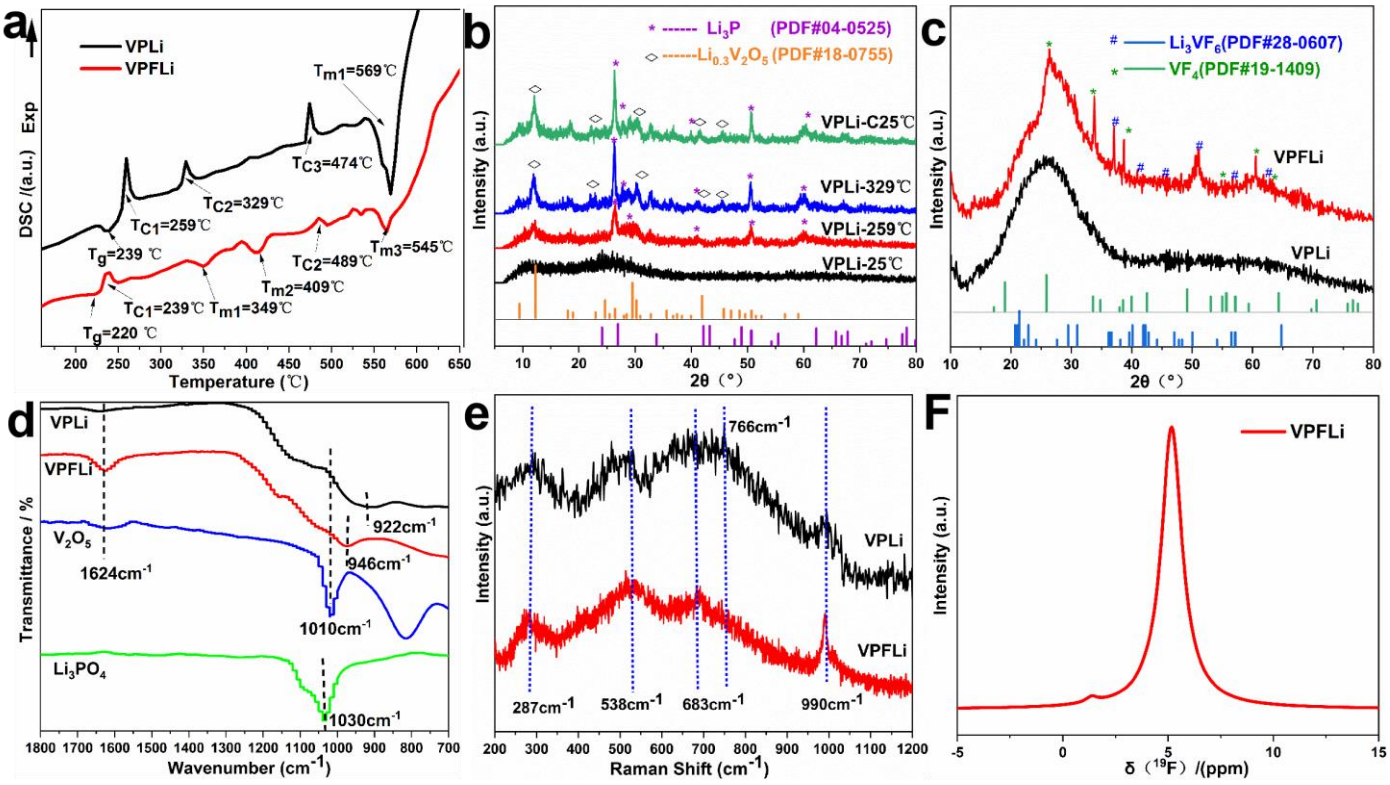

Fig.2. (a) DSC scan of VPLi and VPFLi, (b) *in situ* XRD pattern of VPLi at different temperatures, (c) XRD pattern of VPLi and VPFLi, (d) IR spectra of VPLi, VPFLi, Li_3PO_4, and V_2O_5, (e) Raman spectra of VPLi and VPFLi, and (f) ^{19}F frequency-stepping spectra of VPFLi obtained by solid-state NMR.

SEM images of VPLi and VPFLi are shown in Fig.3(a)-(b). Elements V, P, O and F within VPFLi were identified in the EDS elemental mapping and its associated spectra Fig.3(c)-(d). EDX point analysis confirms the substitution molar ratio of fluorine for oxygen is 1:10. The particle sizes of VPLi and VPFLi are in the range of 2-10 μm according to the analysis using , Fig.3(e). Since F^{-1} ion has a smaller radius (0.133nm) than O^{2-} (0.136nm), it is less prone to the concentration quenching effect [60], and can render a higher doping concentration. The TEM images and the associated SAED patterns suggest VPLi (Fig.3(f))

has a disordered amorphous structure. In contrast,VPFLi (Fig3(g)) features nano-polycrystals embedded in an amorphous phase, which corroborate well with the previous XRD pattern (Fig.2(c)). The insets shown in Fig.3(g1)-(g2) confirm the presence of nanocrystalline regions in VPFLi. The interplanar lattice spacing of 0.344 nm and 0.225 nm correspond to the (111) plane of VF_4 (PDF#19-1409) nanocrystal and (112) plane of Li_3VF_6 (PDF#28-0607) nanocrystal, respectively. Fig.3(h) shows the crystal structures of VF_4 and Li_3VF_6, respectively.

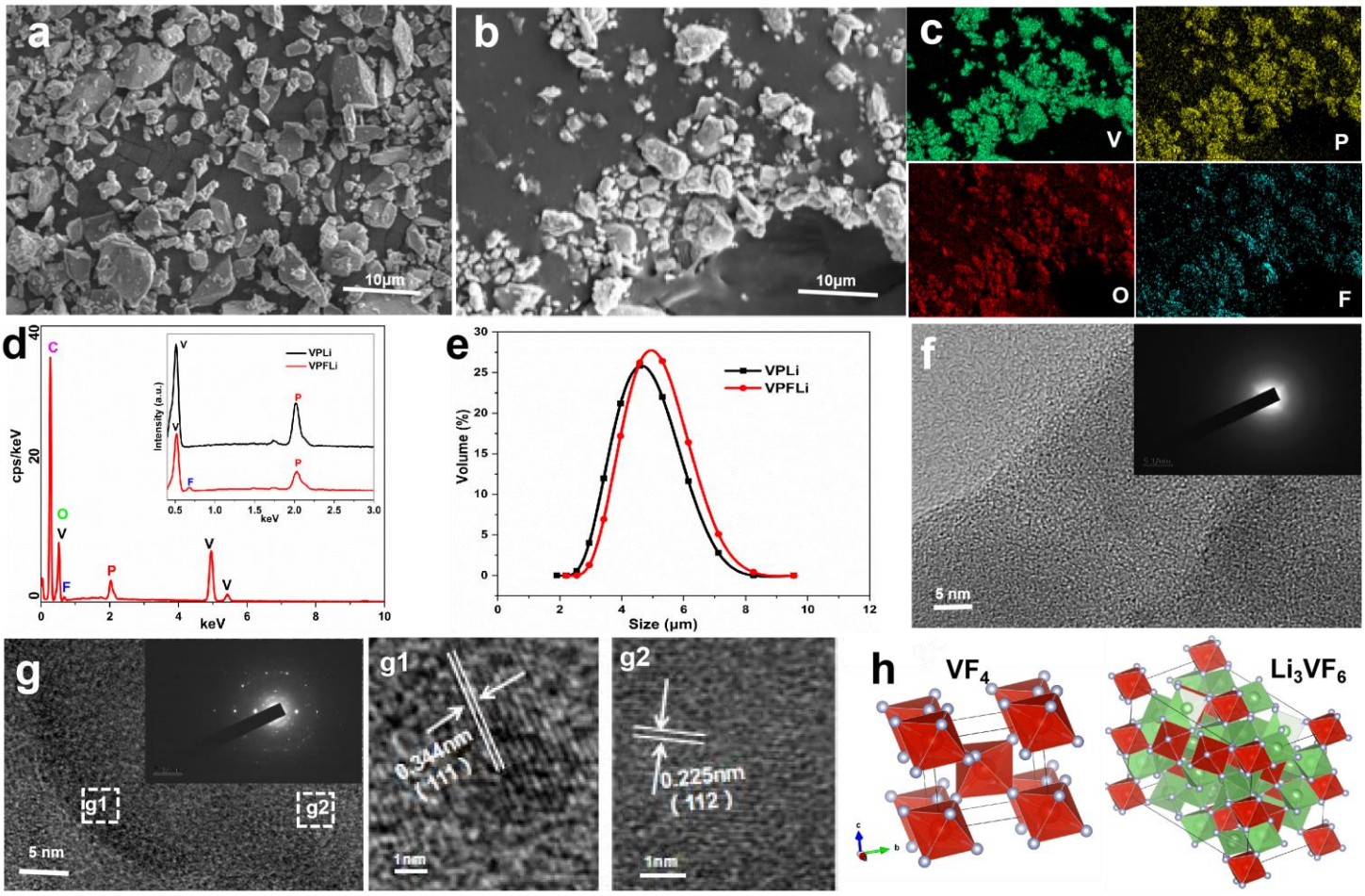

Fig.3. Microstructure and elemental analysis of VPLi and VPFLi. (a) SEM of VPLi, (b) SEM of VPFLi, (c) elemental mapping of VPFLi, (d) EDS of VPFLi (insets: comparison between VPLi and VPFLi), (e) Particle size distribution of VPLi and VPFLi, (f) TEM of VPLi with SAED pattern, (g) TEM of VPFLi with SAED pattern (insets: lattice structure of (g1) (111) plane of VF_4 and (g2) (112) plane of Li_3VF_6,), (h) the crystal structure of VF_4 and Li_3VF_6.

Vanadium usually presents in V^{5+}, V^{4+}, and V^{3+} states in vanadate glass with their respective electronic structures $3p^63d^0$, $3p^63d^1$, and $3p^63d^2$. The electron paramagnetic resonance is an effective technique for detecting V^{4+} [61] as the unpaired electrons surrounding the V^{4+} nucleus can generate strong EPR signals.

VPLi and VPFLi have the same stoichiometry dring the test. Fig.4(a) shows that the EPR peak intensity of VPFLi is ~ 1.46 times greater than that of VPLi, confirming the significantly increased V^{4+}content in VPFLi .

The full spectrum XPS survey (Fig.4(b)) shows that VPFLi contains V*2p*, P*2p*, O*1s*, Li*1s*, C*1s* and F*1s*, and VPLi contains V*2p*, P*2p*, O*1s*, Li*1s* and C*1s*. The relative abundance of P-O-P, V-O-V, Li-O-Li and non-bridging oxygen (NBO) can be found from the high-resolution O*1s* XPS spectra in Fig.4(c) (VPLi), Fig.4(d) (VPFLi) and Table 1. After fluorination, O*1s* of the V-O-V bonds (531.3 eV) reduced significantly from 56.7% to 46.9% and the Li-O-Li bonds (530.6 eV) reduced from 16.2% to 3.9%. This is because, the Li-O-Li structure can induce non-hybridization of the oxygen atomic orbital. The orbital energy level is raised to a level between the transition metal e_g* and t_{2g} levels, which induces the redox reaction of oxygen [56] and triggers the V-F bond formation. In contrast, O*1s* of the P-O-P bonds (532.4 eV) increased significantly from 3.0% to 16% and the NBO bonds (530.9 eV) increased from 8.3% to 10%.

As shown in Fig.4 (e) and (f), the peak position of the V 2p3/2 XPS spectra at 516.5 eV can be assigned to V^{3+}, 517.4 eV to V^{4+}, and 518.1 eV to V^{5+} [48.62] in VPLi and VPFLi. Literature [63] reports that V^{4+} content is related to electrical conductivity. Table 2 shows that after fluorination, V^{3+} content increased from 3.0% to 16.2%, and the V^{4+} content increased from 16.3% to 23.8% with the V^{5+} content decreased from 80.7% to 60.0%, indicating effect of fluorination in reducing the valence state of V. As such, Li_3VF_6 can be considered as an emerging electrochemically active lithium intercalation material [64]. In Li_3VF_6, the substitution of O by F leads to reduced overall number of negative charges. To maintain the material's electrical neutrality, the average valence of V must decrease, which can be achieved by V_2O_5 to V_2O_4 / V_2O_3 conversion during heating of VPLi [65]. From Table 2, it can be seen that the lower valence V is dominated by V_2O_4 and with the greater number of V^{4+} participating in the electrode reaction（V^{4+}/V^{3+}), the electrode's discharge capacity is expanded accordingly. In addition, V_2O_4 has a unique structure consisting of [VO_6] octahedral double layers connected by shared corners, which provides efficient diffusion paths for Li^+ ions

[19].

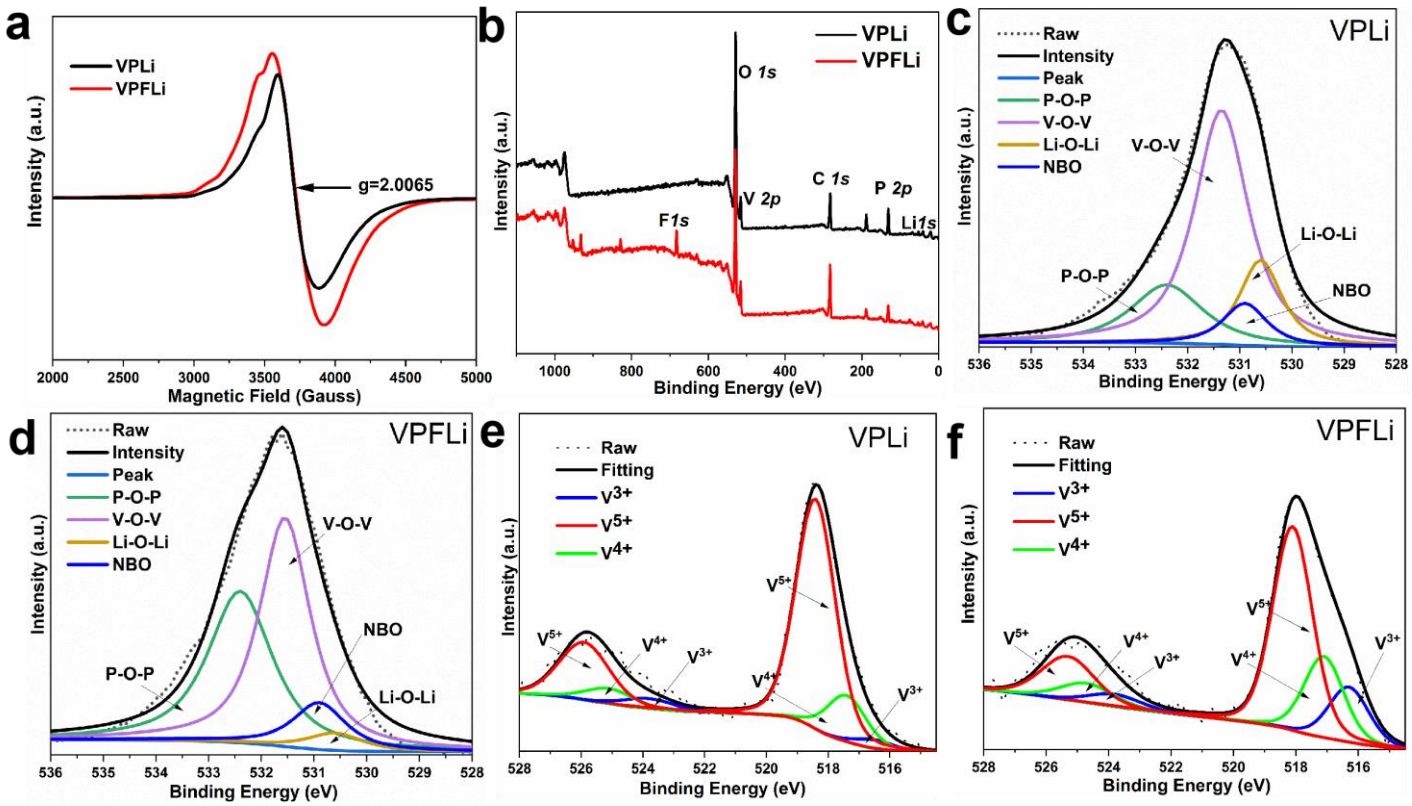

Fig.4. EPR and XPS spectra of VPLi and VPFLi: (a) EPR spectrum survey, (b) XPS full spectrum survey, (c) O*1s* deconvolution for VPLi, (d) O*1s* deconvolution for VPFLi, (e) V *2p* deconvolution for VPLi, (f) V *2p* deconvolution for VPFLi.

Table 1 Relative abundance of P-O-P, V-O-V,Li-O-Li and NBO obtained from high-resolution O *1s* XPS spectra.

	P-O-P		V-O-V		Li-O-Li		NBO		FWHM (eV)	Lorenz-Gaussian ratio(%)
	Main peak(eV)	Area (%)	Main peak(eV)	Area (%)	Main peak(eV)	Area (%)	Main peak(eV)	Area (%)		
VPLi	532.4	18.8	531.3	56.7	530.6	16.2	530.9	8.3	1.25	80
VPFLi		39.2		46.9		3.9		10	1.25	80

Table 2 Relative abundance of V obtained from high-resolution V *2p3/2* /(V *2p1/2* XPS) spectra.

	V^{3+}		V^{4+}		V^{5+}		FWHM (eV)	Lorenz-Gaussian ratio(%)
	Main peak(eV)	Area (%)	Main peak(eV)	Area (%)	Main peak(eV)	Area (%)		
VPLi	516.5/(523.8)	3.0	517.4/(524.7)	16.3	518.1/(525.4)	80.7	1.5/(2)	80
VPFLi		16.2		23.8		60.0	1.5/(2)	80

3.2 Characterization of battery electrochemical performance

The electrochemical performance of CR2016 type coin cells was studied in detail. As shown in Fig.5(a), VPLi provided specific capacities of 180.1, 166.4, 153.2, 137.7 and 125.3 mAh g^{-1} for the 1^{st}, 10^{th}, 20^{th}, 30^{th}, and 50^{th} cycle, respectively, under a current density of 0.1A g^{-1}, within a voltage range of 1.5 - 4.2V. In contrast, VPFLi (Fig.5(b)) presented enhanced specific capacities of 228.9, 210.8, 193.5, 186.7 and 174.7 mAh g^{-1} for the same cycles, under the same conditions. After 50 cycles, the specific capacity retention rates were 76.3% for VPFLi and 69.6% for VPLi, respectively. Fig.5(c) gives the rate performance of the VPLi and VPFLi under various current densities (100, 200, 400, 800 and 100 mA g^{-1}). The discharge capacities of VPLi were 185–173, 157–142, 95–76, 30–19 and 145–135 mAh g^{-1}, respectively and for VPFLi, greater discharge capacities have been observed (228–220, 208–198, 179–165, 120–99 and 210–205 mAh g^{-1}, respectively) under the same testing conditions.

According to the long-term cycling results shown in Fig.5(d), VPLi presented optimal capacities of 266.8 mAh g^{-1}, and 197.6 mAh g^{-1} after 200 cycles at a current density of 50 mA g^{-1} with capacity retention rate 74.0%. VPFLi presented greater optimal capacities of 344.3 mAh g^{-1}, and 269.7 mAh g^{-1} after 200 cycles with the coulombic effciency approaching 100%, at a current density of 50 mA g^{-1} with capacity retention rate 78.3%. The result implies that VPFLi is a promising material for reversible Li^+ storage. Due to the greater electronegativity of F (4.0) as compared to O (3.5), it has a stronger ability to attract electrons, and its resulting covalent bonding strength with V is higher. V-F covalent bond helps to maintain a stable crystal structure during repeated charge/discharge processes, and effectively improves the cycle stability of the VPFLi.

The electrical conductivity of the assembled battery was evaluated by EIS [18]. Fig.5(e) shows that the charge transfer resistance of VPFLi (R_{CT} = 704 Ω) was only half that of VPLi (R_{CT} = 1499.7Ω). This suggests that substituting F for O of VPFLi and the associated increased V^{4+} content can improve the electrical conductivity of the electrode and hence enhance its rate performance. Fig.5 (f) compares the specific capacity values of VPLi and VPFLi with other cathode materials reported in the literature. In

general, the capacity performance of VPFLi is better (particularly at low and high current densities) than the existing amorphous vanadium-based cathode materials, such as H_2-V_2O_5-P_2O_5 [48],V_2O_5–$LiBO_2$ [51],Li_2O-V_2O_5-SiO_2-B_2O_3 [66], C-Li_2O-V_2O_5-P_2O_5 [67], ε-$VOPO_4$ [68], and vanadium-based crystal cathode materials V_2O_5 nanofibers [69] , V_2O_5 nanoribbon [70].

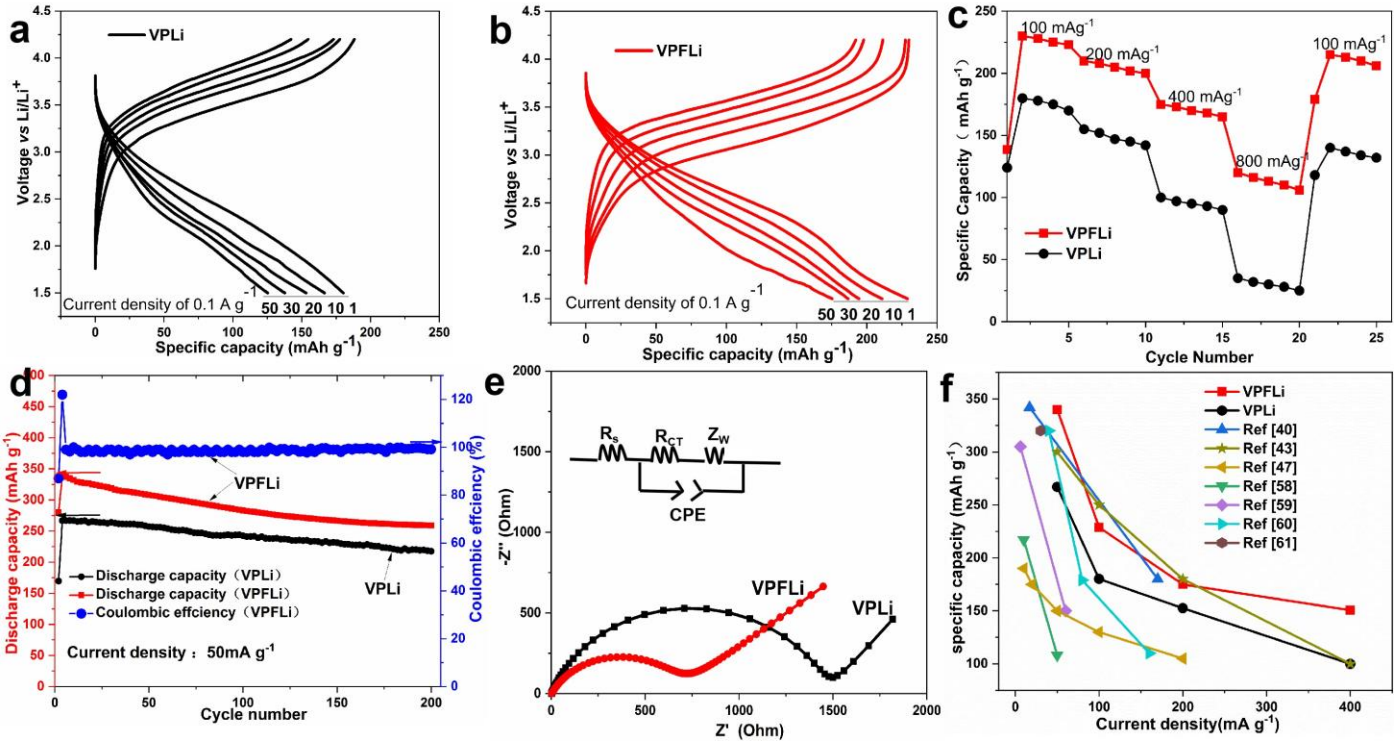

Fig.5. Electrochemical performance of VPLi and VPFLi. (a)-(b) Galvanostatic charge and discharge profiles of VPLi and VPFLi at a current density of 0.1A g^{-1}, (c) Rate performance of VPLi and VPFLi, (d) Long-term cycling of VPFLi, (e) EIS measurements of VPLi and VPFLi, (f) Comparison of specific capacities with reported cathode materials in the literature.

3.3 Lithiation mechanism and DFT calculations

Fig.6(a) shows the CV curves of VPLi and VPFLi at a scan rate of 0.5 mV/s. For VPLi, the peaks at 1.2 V / 0.6V and 3.5 V/ 3.8V can be associated with the redox reaction processes V^{4+}/V^{5+} due to the extraction and insertion of Li^+ [71.72]. The broad peaks at 1.7 V and 2.6V seen for VPFLi can be associated with the redox reaction processes V^{3+}/V^{4+} [68]. Fig.6(b) - (c) shows the *ex situ* XRD spectra of VPLi and VPFLi at different stages of the first charge /discharge cycle at a current rate of 200 mA g^{-1}, *i.e.*, in the initial state (OCV, 3 V), 1.2 (2.6) V (discharge), 0.01 V (discharge), 0.6 (1.7) V (charge), 3.5 V (charge), and 3 V (discharge). As shown in Fig.6(b), nanocrystal $Li_2V_2O_5$ (PDF#48-0076) precipitation within VPLi can be signified by the characteristic peaks at 0.6 V (charge) and 3.5 V (charge). These peaks subsequently disappeared at 3.0 V (discharge) in the first cycle of VPLi. In contrast, $LiVP_2O_7$ (PDF#46-0311) and $Li_2V_2O_5$ (PDF#48-0076)

nanocrystals precipitation was found for VPFLi at 1.7 V (charge) and 3.5 V (charge), which subsequently disappeared at 3.0 V (discharge) in Fig.6(c).

The TEM image of VPLi at 3.5 V (charge) in the first cycle (Fig.6(d)) confirms the material is in a single crystal $Li_2V_2O_5$ state. The inter-planar distance of 0.281 nm in Fig (d1) further confirms it is correlated to the (112) plane of $Li_2V_2O_5$ (PDF#48-0076). The theoretical specific capacity of the V_2O_5 electrode with one Li^+ inserted is 147 mAh g^{-1} and that with two Li^+ inserted is 294 mAh g^{-1} [16]. The specific capacity of VPLi has an intermediate value (180 mAh g^{-1}), see Fig.5(a), which indicates the associated V^{4+}/V^{5+} lithiation process involves conversion of V_2O_5 into $Li_2V_2O_5$ in the first cycle of VPLi [22.73].

On the other hand, the TEM image in Fig.6(e) shows that VPFLi at 3.5 V (charge) is in a polycrystalline state in the first cycle. Fig.(e1) shows the inter-planar distance of 0.656 nm corresponds to the (001) plane of $LiVP_2O_7$（PDF#46-0311. Fig.(e2) shows the inter-planar lattice spacing of 0.323 nm corresponds the (103) plane of $Li_2V_2O_5$ (PDF#48-0076). These results corroborate well with the XDR data in Fig.6(c). Addition of $LiVP_2O_7$ is known to improve the electrode materials capacity and rate performance [74.75], as it can generate a series of V-based multiple redox couples, which offers additional active locations for Li^+ ion storage and effectively shortens the Li^+ ion diffusion pathway. Li^+ is stored in the channel formed by the corner-sharing [VO_6] octahedron and the P_2O_7 group, which is coordinated by four oxygen atoms in the $LiVP_2O_7$ crystal structure [76]. The volume of VPLi and VPFLi remain constant during the Li^+ insertion or extraction process (no significant peak shift in XRD spectra). The reversible peak position and peak intensity in the XRD pattern of VPLi and VPFLi during the charge-discharge cycle indicate both materials are intercalation-type lithium storage materials[77]. The reaction mechanism is shown in Fig.7.

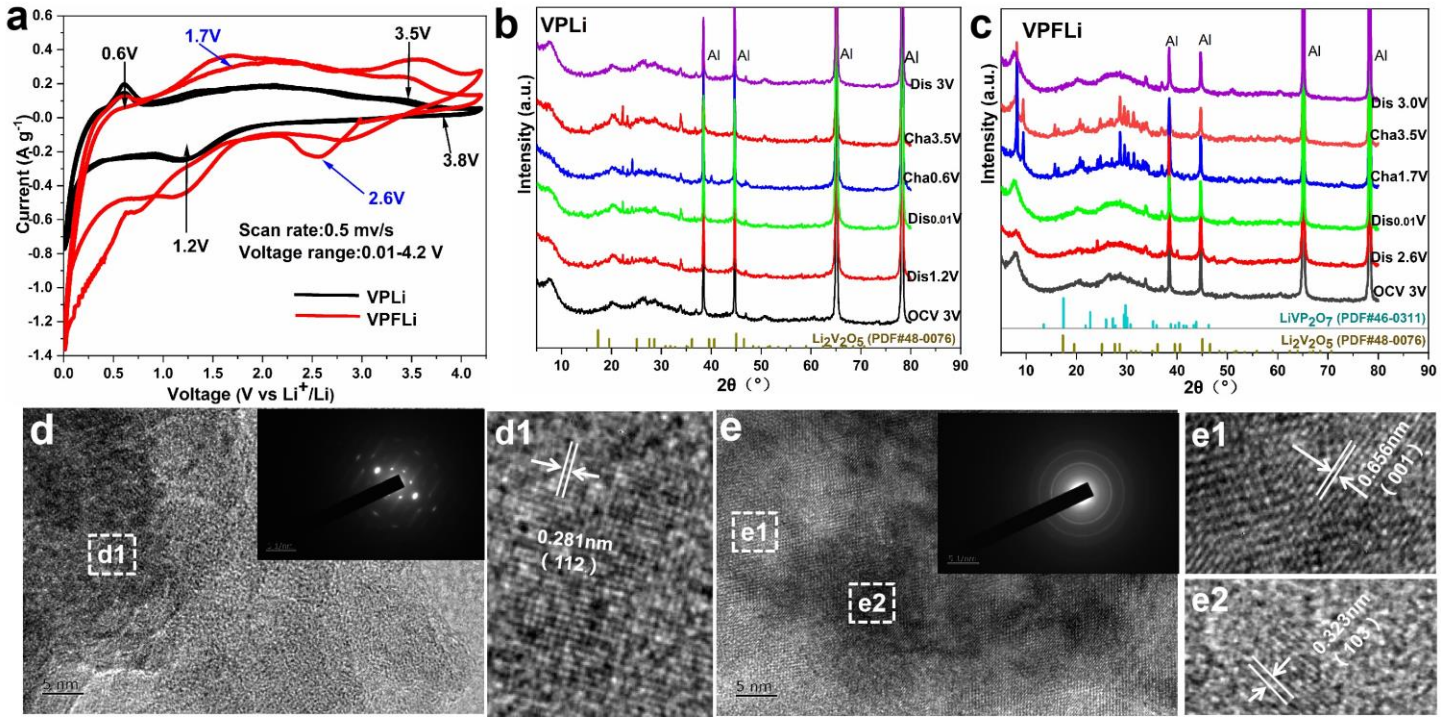

Fig.6. (a) CV curves of VPLi and VPFLi during the first two cycles, (b)-(c) *Ex situ* XRD of VPLi and VPFLi under different charge/ discharge states in the first cycle, (d)-(e) TEM images of VPLi and VPFLi at 3.5 V (charge) in the first cycle (insets: SAED patterns and lattice spacing information).

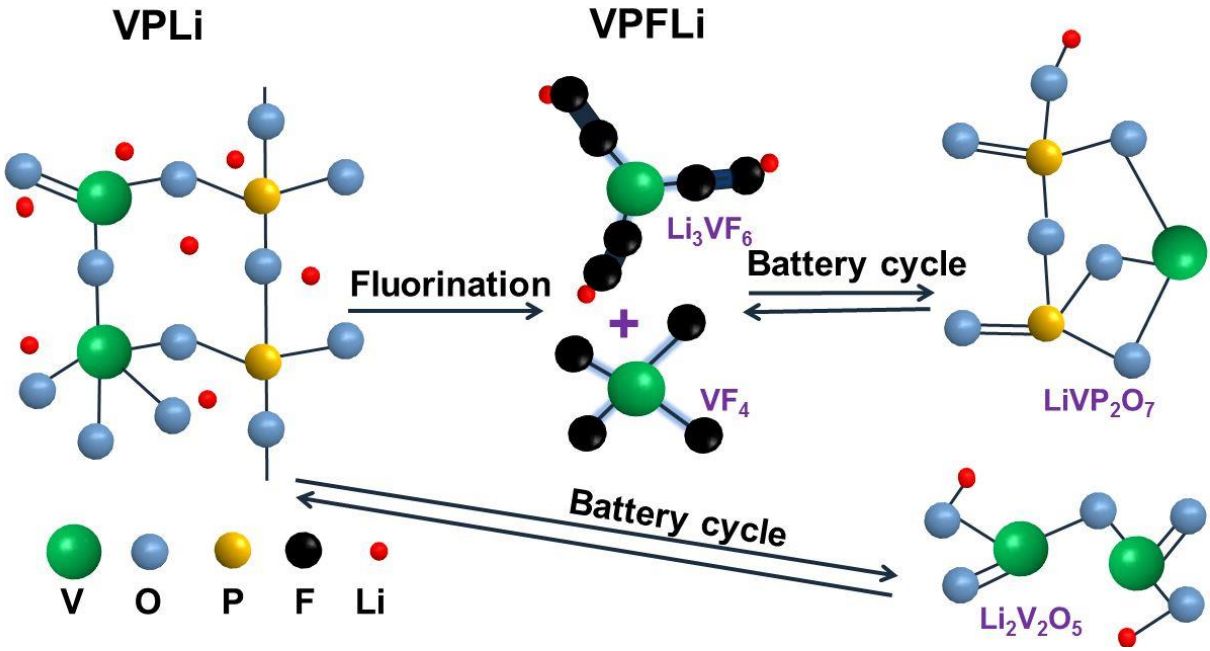

Fig.7. Schematic showing the reaction mechanism during the battery cycles

The presence of nanocrystals within the amorphous glass matrix could lead to a synergistic effect that effectively improve the battery electrical cycle performance [53]. Fluorinated product VPFLi features a polycrystalline structure in which the precipitated Li_3VF_6 and VF_4 nanocrystals were embedded in amorphous phase. Compared to VPLi, VF_4 and Li_3VF_6 crystals were converted into $LiVP_2O_7$ in VPFLi,

296 which led to the increased specific capacity. This is evident by the symmetrical charge/discharge curve and
297 the improved capacity retention rate. It involves reversible order-disorder transition between crystal and
298 amorphous phases during the preparation process and charge-discharge cycles.

299 Density functional theory (DFT) based electronic structure calculations for crystalline vanadium-based
300 electrode materials have been widely reported to date [78.79], and such calculation can reflect the structure
301 stability, the electrons transfer and the atomic bonding within the materials. However, research into
302 amorphous materials such as long/short range disordered structures is still in its infancy. The details of the
303 calculation method based on DFT theoretical model for this study can be found in **Supporting Information**.

304 As shown in Fig.8(a)-(b), the theoretical structural models of VPLi and VPFLi reactants are constructed,
305 which are V_2O_5 and $V_2O_{4.5}F_{0.5}$ (molar ratio O/F=9), respectively. Density of states (DOS) is essentially the
306 number of different states at a specific energy level that electrons are allowed to occupy (the number of
307 electronic states per unit volume per unit energy). Fig.8(c)-(d) display the total density of states of VPLi and
308 VPFLi before and after insertion of a single Li^+. VPLi and VPFLi have semiconductor characteristics with a
309 large characteristic band gap. After a single Li atom was inserted into VPFLi, its Fermi level moves to the
310 edge of the conduction band. This indicates a transition into an n-type semiconductor state as the insertion of
311 Li^+ helps reduce the electrical conductivity and electrode impedance of the structure. Fig.8(e)-(f) show the
312 charge density distribution map of VPLi and VPFLi with a single Li atom insertion, respectively. The
313 simulation result shows the electronic structure (charge accumulation and depletion) and the chemical
314 environment of the lattice structure, which is otherwise difficult to measure experimentally. In VPLi, Li
315 accepts most of the charges transferred from O, while for VPFLi, charges mostly transferred from Li to O
316 due to the presence of F. Therefore, the substitution of fluorine for oxygen contributes to the improvement
317 of the electrical conductivity of the structure and the further reduction of the electrode impedance. Since the
318 battery cycle redox reaction is dependent on reduced oxygen, the reduced irreversible oxygen loss can lead
319 to the imporved cycle stability.

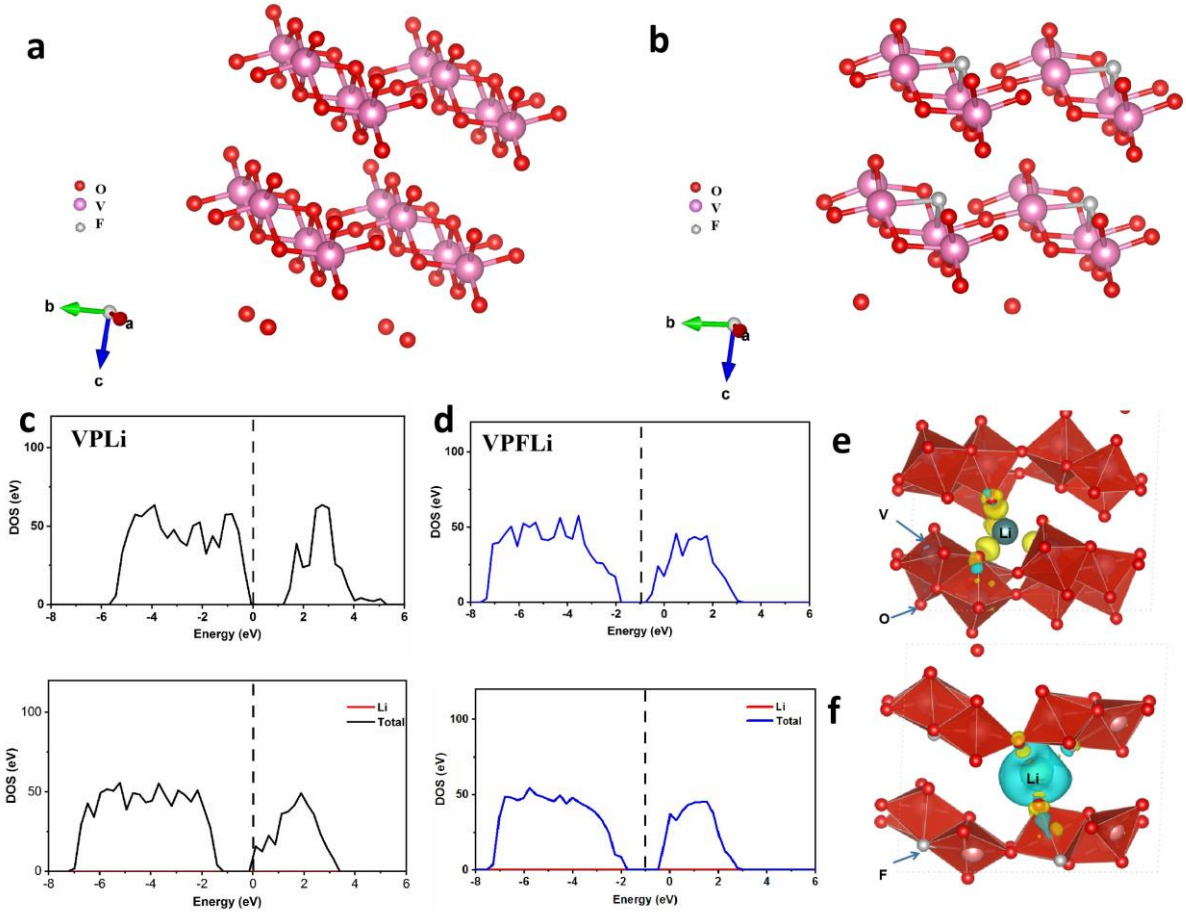

Fig.8. DFT simulation of VPLi and VPFLi for Li ion storage processes. (a)-(b): the theoretical structure models of VPLi and VPFLi, (c)-(d): total density of states of VPLi and VPFLi before and after Li insertion, (e)-(f): charge density difference of VPLi and VPFLi after single Li atom insertion (light blue: charge depletion; yellow: charge accumulation).

4. Conclusions

This work presents the first investigation on a fluorinated vanadium-phosphorus amorphous lithium battery cathode material and the associated structure-performance relationship. After fluorination, the V^{4+} content in the cathode material increased from 16.3% to 23.8%. The fluorinated product VPFLi consists of 10% of precipitates (Li_3VF_6 and VF_4 nanocrystals) and shows an optimal specific capacity of 344.3 mAh g^{-1} in the first cycle and 269.7 mAh g^{-1} after 200 cycles at a current density of 50 mA g^{-1} within a voltage range of 1.5-4.2V. The charge transfer resistance of VPFLi (R_{CT} = 704 Ω) was only half that of VPLi (R_{CT} = 1499.7Ω). Modelling through density functional theory shows that that fluorination contributes to the moving of Fermi level towards the edge of the conduction band, and that charges mostly transferred from Li to O, which led to improved cycle stability.

The lithiation process (V^{4+}/V^{5+}) in amorphous VPLi can be related to the conversion of V_2O_5 to $Li_2V_2O_5$

in the cycling process. Compared to VPLi, VF_4 and Li_3VF_6 crystals were converted into $LiVP_2O_7$ in VPFLi, which increased the specific capacity.It is believed that having VF_4 and Li_3VF_6 nanocrystals embedded in the amorphous glass matrix and the associated order-disorder transition between crystal and amorphous phases can lead to a synergistic effect that enhances the electrical cycle performance of fluorinated vanadium-phosphorus amorphous cathode in practical lithium ion battery applications. This study provides a new perspective towards selecting novel cathode material for future lithium-ion batteries.

Declarations of interest

The authors declare that they have no known competing financial interests or personal relationships that could have appeared to influence the work reported in this paper.

Acknowledgements

This work was supported by the Natural Science Foundation of Hainan Province (519MS022), the Key Scientific & Technological Project of Hainan Province (ZDYF2020015), the Research Lab construction of Hainan University (ZY2019HN09) and the China Scholarship Council under Grant 202107565023.

References:

[1]T. Sadhasivam, M. Park, J. Shim, J. Jin, S. Kim, M.D. Kurkuri, S. Roh, H. Jung, High charge acceptance through interface reaction on carbon coated negative electrode for advanced lead-carbon battery system, ELECTROCHIM. ACTA, 295(2019) 367-375.

[2]T. Sadhasivam, G. Palanisamy, S. Roh, M.D. Kurkuri, S.C. Kim, H. Jung, Electro-analytical performance of bifunctional electrocatalyst materials in unitized regenerative fuel cell system, INT. J. HYDROGEN ENERG., 43(2018) 18169-18184.

[3]G. Palanisamy, H. Jung, T. Sadhasivam, M.D. Kurkuri, S.C. Kim, S. Roh, A comprehensive review on microbial fuel cell technologies: Processes, utilization, and advanced developments in electrodes and membranes, J. CLEAN. PROD., 221(2019) 598-621.

[4]H. Jung, K. Cho, K.A. Sung, W. Kim, M. Kurkuri, J. Park, Sulfonated poly(arylene ether sulfone) as an electrode binder for direct methanol fuel cell, ELECTROCHIM. ACTA, 52(2007) 4916-4921.

[5]R. Com, Global Energy Harvesting System Market Outlook 2019-2027 - Drivers, Constraints, Opportunities, Threats, Challenges, Investment Opportunities, 2021. https://finance.yahoo.com/news/global-energy-harvesting-system-market-100700710.html

[6]G. Lee, Y. Seon Kim, M. Sung, D. Kim, Ultrafine CoP nanoparticles encapsulated in N/P dual-doped carbon cubes derived from 7,7,8,8-tetracyanoquinodimethane for lithium-ion batteries, APPL. SURF. SCI., 555(2021) 149716.

[7]K. Zhang, Y. Tian, C. Wei, Y. An, J. Feng, Building stable solid electrolyte interphases (SEI) for microsized silicon anode and 5V-class cathode with salt engineered nonflammable phosphate-based lithium-ion battery electrolyte, APPL. SURF. SCI., 553(2021) 149566.

[8]C. Zhou, P. Zhang, W. Wang, Y. Yang, W. Wang, H. Ding, X. Xu, W. Ji, L. Chen, Hierarchical modulation of NiSe2

nanosheets/nanodendrites by phase engineering on N-doped 3D porous graphene as self-supporting anode for superior lithium ion batteries, APPL. SURF. SCI., (2021) 150784.
[9]M. He, L. Zhang, J. Li, Theoretical investigation on interactions between lithium ions and two-dimensional halide perovskite for solar-rechargeable batteries, APPL. SURF. SCI., 541(2021) 148509.
[10]J. Wang, X. Sun, Understanding and recent development of carbon coating on LiFePO4 cathode materials for lithium-ion batteries, ENERG ENVIRON SCI, 5(2012) 5163-5185.
[11]S. Neudeck, F. Walther, T. Bergfeldt, C. Suchomski, M. Rohnke, P. Hartmann, J. Janek, T. Brezesinski, Molecular Surface Modification of NCM622 Cathode Material Using Organophosphates for Improved Li-Ion Battery Full-Cells, ACS APPL MATER INTER, 10(2018) 20487-20498.
[12]W. Oh, H. Park, B. Jin, R. Thangavel, W. Yoon, Understanding the structural phase transitions in lithium vanadium phosphate cathodes for lithium-ion batteries, J. MATER CHEM A, 8(2020) 10331-10336.
[13]R. Thangavel, K. Kaliyappan, K. Kang, X. Sun, Y.S. Lee, Going Beyond Lithium Hybrid Capacitors: Proposing a New High - Performing Sodium Hybrid Capacitor System for Next - Generation Hybrid Vehicles Made with Bio - Inspired Activated Carbon, ADV ENERGY MATER, 6(2016) 1502199.
[14]Y. Subramanian, W. Oh, W. Choi, H. Lee, M. Jeong, R. Thangavel, W. Yoon, Optimizing high voltage Na3V2(PO4)2F3 cathode for achieving high rate sodium-ion batteries with long cycle life, CHEM. ENG. J., 403(2021) 126291.
[15]M.S. Whittingham, Lithium Batteries: 50 Years of Advances to Address the Next 20 Years of Climate Issues, NANO LETT., 20(2020) 8435-8437.
[16]Y. Yue, H. Liang, Micro - and Nano - Structured Vanadium Pentoxide (V2O5) for Electrodes of Lithium - Ion Batteries, ADV ENERGY MATER, 7(2017) 1602541-1602545.
[17]X. Xu, F. Xiong, J. Meng, Q. An, L. Mai, Multi-electron reactions of vanadium-based nanomaterials for high-capacity lithium batteries: challenges and opportunities, Materials Today Nano, 10(2020) 100073.
[18]J. Cao, D. Zhang, Y. Yue, X. Wang, T. Pakornchote, T. Bovornratanaraks, X. Zhang, Z. Wu, J. Qin, Oxygen defect enriched (NH4)2V10O25 8H2O nanosheets for superior aqueous zinc - ion batteries, NANO ENERGY, 84(2021) 105876.
[19]Y. Zhu, M. Yang, Q. Huang, D. Wang, R. Yu, J. Wang, Z. Zheng, D. Wang, V2O5 Textile Cathodes with High Capacity and Stability for Flexible Lithium - Ion Batteries, Advanced materials, 32(2020) 1906205.
[20]S. Zhang, H. Tan, X. Rui, Y. Yu, Vanadium-Based Materials: Next Generation Electrodes Powering the Battery Revolution? ACCOUNTS CHEM. RES., (2020) 1660-1671.
[21]Y. Liu, Z. Sun, X. Sun, Y. Lin, C. Yuan, Construction of ultrathin V3S4@C nanosheets assembled hierarchical nanotubes towards alkali on batteries with ion ependent electrochemical mechanisms, Angewandte Chemie International Edition, 132(2020) 2494-2503.
[22]C. Delmas, H. Cognac-Auradou, J.M. Cocciantelli, M. Ménétrier, J.P. Doumerc, The LixV2O5 system: An overview of the structure modifications induced by the lithium intercalation, SOLID STATE IONICS, 69(1994) 257-264.
[23]Y. Xu, M. Dunwell, L. Fei, E. Fu, Q. Lin, B. Patterson, B. Yuan, S. Deng, P. Andersen, H. Luo, G. Zou, Two-Dimensional V2O5 Sheet Network as Electrode for Lithium-Ion Batteries, ACS APPL MATER INTER, 6(2014) 20408-20413.
[24]C. Zhang, Z. Chen, Z. Guo, X.W.D. Lou, Additive-free synthesis of 3D porous V2O5 hierarchical microspheres with enhanced lithium storage properties, ENERG ENVIRON SCI, 6(2013) 974-978.
[25]J. Lee, D.A. Kitchaev, D.H. Kwon, C.W. Lee, J.K. Papp, Y.S. Liu, Z. Lun, R.J. Clement, T. Shi, B.D. Mccloskey, Reversible Mn2+/Mn4+ double redox in lithium-excess cathode materials, NATURE, 556(2018) 185-190.
[26]D.A. Kitchaev, Z. Lun, W.D. Richards, H. Ji, R.J. Clément, M. Balasubramanian, D. Kwon, K. Dai, J.K. Papp, T. Lei, B.D. McCloskey, W. Yang, J. Lee, G. Ceder, Design principles for high transition metal capacity in disordered rocksalt Li-ion cathodes, ENERG ENVIRON SCI, 11(2018) 2159-2171.
[27]R.J. Clément, Z. Lun, G. Ceder, Cation-disordered rocksalt transition metal oxides and oxyfluorides for high energy lithium-ion cathodes, ENERG ENVIRON SCI, 13(2020) 345-373.
[28]H. Song, M. Luo, A. Wang, High Rate and Stable Li-Ion Insertion in Oxygen-Deficient LiV3O8 Nanosheets as a Cathode Material for Lithium-Ion Battery, ACS APPL MATER INTER, 9(2017) 2875-2882.
[29]D. Seo, J. Lee, A. Urban, R. Malik, S. Kang, G. Ceder, The structural and chemical origin of the oxygen redox activity in layered and cation-disordered Li-excess cathode materials, NAT CHEM, 8(2016) 692-697.
[30]L. Du, H. Lin, Z. Ma, Q. Wang, D. Li, Y. Shen, W. Zhang, K. Rui, J. Zhu, W. Huang, Using and recycling V2O5 as high

418 performance anode materials for sustainable lithium ion battery, J. POWER SOURCES, 424(2019) 158-164.
419 [31]Z. Wang, H. Huang, L. Zeng, Y. Wang, D. Fang, In-operando deformation studies on the mechano-electrochemical
420 mechanism in free-standing MWCNTs/V2O5 lithium ion battery electrode, ELECTROCHIM. ACTA, 305(2019) 101-115.
421 [32]D. Kong, X. Li, Y. Zhang, X. Hai, B. Wang, X. Qiu, Q. Song, Q. Yang, L. Zhi, Encapsulating V2O5 into carbon nanotubes
422 enables the synthesis of flexible high-performance lithium ion batteries, ENERG ENVIRON SCI, 9(2016) 906-911.
423 [33]F. Ye, D. Lu, X. Gui, T. Wang, X. Zhuang, W. Luo, Y. Huang, Atomic layer deposition of core-shell structured V2O5@CNT
424 sponge as cathode for potassium ion batteries, Journal of Materiomics, 5(2019) 344-349.
425 [34]R. Chen, R. Luo, Y. Huang, F. Wu, L. Li, Advanced High Energy Density Secondary Batteries with Multi‐Electron
426 Reaction Materials, ADV SCI, 3(2016) 1600051.
427 [35]X. Xu, F. Xiong, J. Meng, Q. An, L. Mai, Multi-electron reactions of vanadium-based nanomaterials for high-capacity lithium
428 batteries: challenges and opportunities, Materials Today Nano, (2020) 100073.
429 [36]Y. Huang, F. Wu, R. Chen, Thermodynamic analysis and kinetic optimization of high-energy batteries based on
430 multi-electron reactions, NATL SCI REV, 7(2020) 1367-1386.
431 [37]Z. Zhou, J. Zhang, S. Chen, H. Yao, Y. Dong, The electrochemical performanceand multielectron reaction mechanism of
432 NiV2O6 as anovel anode material for lithium-ion batteries, ELECTROCHIM. ACTA, (2020) 136979.
433 [38]H. Song, C. Liu, C. Zhang, G. Cao, Self-doped V4+‐V2O5 nanoflake for 2 Li-ion intercalation with enhanced rate and
434 cycling performance, NANO ENERGY, 22(2016) 1-10.
435 [39]S. Ni, X. Lv, J. Ma, X. Yang, L. Zhang, Electrochemical characteristics of lithium vanadate Li3VO4 as a new sort of anode
436 material for Li-ion batteries, J. POWER SOURCES, 248(2014) 122-129.
437 [40]X. Sun, C. Zhou, M. Xie, T. Hu, H. Sun, G. Xin, G. Wang, S.M. George, J. Lian, Amorphous vanadium oxide coating on
438 graphene by atomic layer deposition for stable high energy lithium ion anodes, CHEM. COMMUN., 50(2014) 10703-10706.
439 [41]O.B. Chae, J. Kim, I. Park, H. Jeong, J.H. Ku, J.H. Ryu, K. Kang, S.M. Oh, Reversible Lithium Storage at Highly Populated
440 Vacant Sites in an Amorphous Vanadium Pentoxide Electrode, CHEM. MATER., 26(2014) 5874-5881.
441 [42]J.G. Smith, D.J. Siegel, Low-temperature paddlewheel effect in glassy solid electrolytes, NAT COMMUN, 11(2020) 1483.
442 [43]R. Garcia Mendez, J.G. Smith, J.C. Neuefeind, D.J. Siegel, J. Sakamoto, Correlating Macro and Atomic Structure with Elastic
443 Properties and Ionic Transport of Glassy Li2S‐P2S5 (LPS) Solid Electrolyte for Solid‐State Li Metal Batteries, ADV
444 ENERGY MATER, 10(2020) 2000335.
445 [44]F. Han, A.S. Westover, J. Yue, X. Fan, F. Wang, M. Chi, D.N. Leonard, N.J. Dudney, H. Wang, C. Wang, High electronic
446 conductivity as the origin of lithium dendrite formation within solid electrolytes, NAT ENERGY, 4(2019) 187-196.
447 [45]Y. Zhang, Glass anodes for lithium ion batteries: Insight from the structural evolution during discharging/charging, INT J.
448 APPL GLASS SCI, 11(2020) 577-589.
449 [46]Z. Jiang, T. Zhao, J. Ren, Y. Zhang, Y. Yue, NMR evidence for the charge-discharge induced structural evolution in a Li-ion
450 battery glass anode and its impact on the electrochemical performances, NANO ENERGY, 80(2021) 105589.
451 [47]F. Xiong, Q. An, L. Xia, Y. Zhao, L. Mai, H. Tao, Y. Yue, Revealing the atomistic origin of the disorder-enhanced Na-storage
452 performance in NaFePO4 battery cathode, NANO ENERGY, 57(2019) 608-615.
453 [48]M. Du, K. Huang, Y. Guo, Z. Xie, H. Jiang, C. Li, Y. Chen, High specific capacity lithium ion battery cathode material
454 prepared by synthesizing vanadate‐phosphate glass in reducing atmosphere, J. POWER SOURCES, 424(2019) 91-99.
455 [49]F. Kong, X. Liang, L. Yi, X. Fang, Z. Yin, Y. Wang, R. Zhang, L. Liu, Q. Chen, M. Li, C. Li, H. Jiang, Y. Chen,
456 Multi-electron reactions for the synthesis of a vanadium-based amorphous material as lithium-ion battery cathode with high
457 specific capacity, ENERGY, 219(2021) 119513.
458 [50]T.S. Arthur, K. Kato, J. Germain, J. Guo, P. Glans, Y. Liu, D. Holmes, X. Fan, F. Mizuno, Amorphous V2O5‐P2O5 as
459 high-voltage cathodes for magnesium batteries, CHEM. COMMUN., 51(2015) 15657-15660.
460 [51]S. Afyon, F. Krumeich, C. Mensing, A. Borgschulte, R. Nesper, New High Capacity Cathode Materials for Rechargeable
461 Li-ion Batteries: Vanadate-Borate Glasses, SCI REP-UK, 4(2015) 7113.
462 [52]Y. Zhang, P. Wang, G. Li, J. Fan, C. Gao, Z. Wang, Y. Yue, Clarifying the charging induced nucleation in glass anode of
463 Li-ion batteries and its enhanced performances, NANO ENERGY, 57(2018) 592-599.
464 [53]Y. Zhang, P. Wang, T. Zheng, D. Li, G. Li, Y. Yue, Enhancing Li-ion battery anode performances via disorder/order
465 engineering, NANO ENERGY, 49(2018) 596-602.
466 [54] J. Fan, Y. Zhang, G. Li, Y. Yue, Tellurium nanoparticles enhanced electrochemical performances of TeO2-V2O5-Al2O3

glass anode for Lithium-ion batteries, J. NON-CRYST. SOLIDS, 521(2019) 119491.
[55]E. Zhao, S. Zhao, X. Wu, J. Li, L. Yu, C. Nan, G. Cao, Electrochemical performance of Li2O-V2O5-SiO2-B2O3 glass as cathode material for lithium ion batteries, Journal of Materiomics, 5(2019) 663-669.
[56]D. Seo, J. Lee, A. Urban, R. Malik, S. Kang, G. Ceder, The structural and chemical origin of the oxygen redox activity in layered and cation-disordered Li-excess cathode materials, NAT CHEM, 8(2016) 692-697.
[57]S. Mandal, S. Hazra, D. Das, A. Ghosh, Structural studies of binary iron vanadate glass, J. NON-CRYST. SOLIDS, 183(1995) 315-319.
[58]S. Ibrahim, M.A. Marzouk, G.M. El Komy, Structural Characteristics and Electrical Conductivity of Vanadium-doped lithium Ultraphosphate Glasses, SILICON-NETH, 9(2017) 403-410.
[59]F. Fu, K. Liao, J. Ma, Z. Cheng, D. Zheng, L. Gao, C. Liu, S. Li, W. Li, How intermolecular interactions influence electronic absorption spectra: insights from the molecular packing of uracil in condensed phases, PHYS. CHEM. CHEM. PHYS., 21(2019) 4072-4081.
[60]W.B. Jensen, The Origin of the Ionic-Radius Ratio Rules, J. CHEM. EDUC., 87(2010) 587-588.
[61]L.D. Bogomolova, T.F. Dolgolenko, V.A. Tachkin, V.N. Lazukin, The EPR of V4+ and Cu2+ ions as a method of the study of glass structure, Journal of Magnetic Resonance (1969), 15(1974) 283-291.
[62]L. Yu, S. Zhao, X. Wu, J. Li, E. Zhao, G. Wei, Lithium ion storage behaviors of (100-x) V2O5-(x) P2O5 glass as novel anode materials for lithium ion battery, J. ALLOY. COMPD, 810(2019) 151938.
[63]P. Nagels, Electronic transport in amorphous semiconductors,Springer Berlin Heidelberg, Berlin, Heidelberg, 1985, 113-158.
[64]A. Basa, E. Gonzalo, A. Kuhn, F. Garc á-Alvarado, Facile synthesis of β-Li3VF6: A new electrochemically active lithium insertion material, J. POWER SOURCES, 207(2012) 160-165.
[65]R. Dziembaj, J. Piwowarczyk, Oxygen equilibrium pressure above the V2O5 − x oxide system at 600 ℃ (x < 0.43), J. SOLID STATE CHEM., 21(1977) 387-392.
[66]Z. En-Lai, Z. Shi-Xi, W. Xia, L. Jing-Wei, C. Guozhong, Electrochemical performance of Li2O-V2O5-SiO2-B2O3 glass as cathode material for lithium ion batteries, Journal of Materiomics, 5(2019) 663-669.
[67]L. Jingwei, Z. Shixi, W. Xia, Y. Lüqiang, Z. Enlai, N. Cewen, Structure and electrochemical properties of C-coated Li2O – V2O5 – P2O5 glass-ceramic as cathode material for lithium-ion batteries, FUNCT MATER LETT, 12(2019) 1951002.
[68]C. Siu, I.D. Seymour, S. Britto, H. Zhang, J. Rana, J. Feng, F.O. Omenya, H. Zhou, N.A. Chernova, G. Zhou, C.P. Grey, L.F.J. Piper, M.S. Whittingham, Enabling multi-electron reaction of ε-VOPO4 to reach theoretical capacity for lithium-ion batteries, CHEM. COMMUN., 54(2018) 7802-7805.
[69]Y.L. Cheah, N. Gupta, S.S. Pramana, V. Aravindan, G. Wee, M. Srinivasan, Morphology, structure and electrochemical properties of single phase electrospun vanadium pentoxide nanofibers for lithium ion batteries, J. POWER SOURCES, 196(2011) 6465-6472.
[70]J. Zhu, H. Shen, X. Shi, F. Yang, X. Hu, W. Zhou, H. Yang, M. Gu, Revealing the Chemical and Structural Evolution of V2O5 Nanoribbons in Lithium-Ion Batteries Using in Situ Transmission Electron Microscopy, ANAL. CHEM., 91(2019) 11055-11062.
[71]W. Zhong, J. Huang, S. Liang, J. Liu, Y. Jiang, New Prelithiated V 2 O 5 Superstructure for Lithium-Ion Batteries with Long Cycle Life and High Power, ACS ENERGY LETT, 1(2020) 31-38.
[72]A. Pan, H.B. Wu, L. Yu, T. Zhu, X.W.D. Lou, Synthesis of Hierarchical Three-Dimensional Vanadium Oxide Microstructures as High-Capacity Cathode Materials for Lithium-Ion Batteries, ACS APPL MATER INTER, 4(2012) 3874-3879.
[73]J.B. Lee, J. Moon, O.B. Chae, J.G. Lee, J.H. Ryu, M. Cho, K. Cho, S.M. Oh, Unusual Conversion-type Lithiation in LiVO3 Electrode for Lithium-Ion Batteries, CHEM. MATER., 28(2016) 5314-5320.
[74]V. Mani, N. Kalaiselvi, LiVP2O7/C: A New Insertion Anode Material for High-Rate Lithium-Ion Battery Applications, INORG. CHEM., 55(2016) 3807-3814.
[75]J. Barker, R. Gover, P. Burns, A. Bryan, LiVP2O7: A viable lithium-ion cathode material? Electrochemical and Solid State Letters - ELECTROCHEM SOLID STATE LETT, 8(2005) A446. https://doi.org/10.1149/1.1979347
[76]K.H. Lii, Y.P. Wang, Y.B. Chen, S.L. Wang, The crystal structure of LiVP2O7, J. SOLID STATE CHEM., 86(1990) 143-148.

[77]R. Li, G. Liang, X. Zhu, Q. Fu, Y. Chen, L. Luo, C. Lin, Mo3Nb14O44: A New Li+ Container for High‐Performance Electrochemical Energy Storage, ENERGY & ENVIRONMENTAL MATERIALS, 4(2021) 65-71.
[78]T. Wu, K. Zhu, C. Qin, K. Huang, Unraveling the role of structural water in bilayer V2O5 during Zn2+ intercalation: insights from DFT calculations, J. MATER CHEM A, 7(2019) 5612-5620.
[79]A. Xu, L. Shi, L. Zeng, T.S. Zhao, First-principle investigations of nitrogen-, boron-, phosphorus-doped graphite electrodes for vanadium redox flow batteries, ELECTROCHIM. ACTA, 300(2019) 389-395.